

## Optical and analytical transmission-electron-microscopy studies of thermochemically reduced MgO crystals

C. Ballesteros

*Departamento de Física del Estado Sólido, Facultad de Ciencias Físicas, Universidad Complutense, 28040 Madrid, Spain  
and Solid State Division, Oak Ridge National Laboratory, Oak Ridge, Tennessee 37831*

R. González

*Department of Materials Engineering, North Carolina State University, Raleigh, North Carolina 27695  
Departamento de Física del Estado Sólido, Facultad de Ciencias Físicas, Universidad Complutense, 28040 Madrid, Spain  
and Solid State Division, Oak Ridge National Laboratory, Oak Ridge, Tennessee 37831*

S. J. Pennycook and Y. Chen

*Solid State Division, Oak Ridge National Laboratory, Oak Ridge, Tennessee 37831  
(Received 29 January 1988)*

MgO crystals from five sources were thermochemically reduced at high temperatures. Optical-absorption measurements indicated that anion vacancies were present in all of the crystals. In addition, crystal darkening was observed and was due to a broad absorption in the visible region. The dark coloration was impurity related. Analytical transmission-electron-microscopy techniques indicated the presence of metallic precipitates that were primarily Fe in content. Microdiffraction patterns indicated that the precipitates possessed the fcc ( $a_0 = 3.61 \text{ \AA}$ ) or the bcc ( $a_0 = 2.89 \text{ \AA}$ ) crystal structure. The fcc precipitates were found to have a matrix relationship of  $\langle 001 \rangle_p \parallel \langle 001 \rangle_m$  and  $\langle 010 \rangle_p \parallel \langle 010 \rangle_m$ . The bcc precipitates were found to have a relationship of  $\langle 001 \rangle_p \parallel \langle 001 \rangle_m$  and  $\langle 110 \rangle_p \parallel \langle 010 \rangle_m$ .

### I. INTRODUCTION

Thermochemical reduction (TCR) is one of two viable methods to produce vacancies in refractory oxides for use in optical devices,<sup>1</sup> the other being particle irradiation.<sup>2,3</sup> This technique involves heating the material at very high temperatures in an oxygen-deficiency atmosphere to produce oxygen vacancies. The resulting vacancies have the advantage in that they are thermally stable and emit broad luminescence with high quantum efficiencies. However, TCR can cause precipitation of impurities, causing attenuation of light in the crystals.<sup>4-6</sup>

Whereas precipitates have been observed and studied in thermochemically reduced MgO crystals doped with different impurities, nominally pure MgO crystals, to our knowledge, have not been characterized. There exists a wide range of impurity contents in nominally pure MgO crystals. In this work, undoped MgO crystals were obtained from five sources. After TCR, optical characterization was performed and precipitates in the crystals were characterized using analytical electron microscopy. Transmission-electron-microscopy (TEM) studies on dislocation loops were also performed.

### II. EXPERIMENTAL PROCEDURES

Magnesium oxide crystals were obtained from five sources: Norton Chemical Company (N); Muscle-Shoals Electrochemical Corporation, Muscle-Shoals, Alabama (MS); Tateho Chemical Industry Co., Ltd., Hyogen-Ken, Japan (T); W. C. Spicer Ltd., Gloucestershire, England,

(S); and Oak Ridge (OR). They were all grown by the arc-fusion method. The OR crystals were grown by a variation of this technique that gives large crystals of high purity.<sup>7</sup> The starting material was high-purity MgO powder from the Kanto Chemical Co., Tokyo, Japan. Typical chemical analyses have been reported previously.<sup>8</sup> Crystals from the other four sources were characterized chemically (see Sec. III).

Single crystals having  $\{100\}$  faces with typical dimensions of  $\sim 1 \times 1 \times 0.2 \text{ cm}^3$  were enclosed in an evacuated metal chamber bomb containing magnesium vapor, heated to temperatures of about 2000 K for three hours and then cooled. The samples for electron microscopy were prepared by a jet polishing technique using phosphoric acid at 410 K. Philips EM 400 T and JEOL 100 U transmission electron microscopes were used in this investigation.

The x-ray microanalysis and the diffraction studies of individual precipitates were carried out in a Philips EM-400T analytical electron microscope. The twin-lens design results in electron probe diameters as small as 10 nm in microprobe mode. Thus it is possible to obtain diffraction information (hereafter designated as microdiffraction) from areas significantly smaller than the  $\sim 300 \text{ nm}$  diameter required in the selected-area diffraction technique used in conventional transmission electron microscopy.<sup>9</sup>

Near infrared, visible, and uv measurements were made in a Cary 17D or a Perkin-Elmer, Lambda 9 spectrophotometer. Luminescence experiments were performed in a Spex Fluorometer model 212.

### III. RESULTS AND DISCUSSION

#### A. Chemical analysis

Neutron activation analyses were made on Norton, Muscle-Shoals, and Tateho samples. The impurity analysis is given in Table I; the values for Spicer and Oak Ridge samples were taken from Ref. 8.

#### B. Optical measurements

##### 1. Absorption spectra

The optical-absorption spectra of a Norton sample before and after TCR are shown in Fig. 1. The main feature of the as-grown crystal spectrum is the 290-nm (4.3-eV) band due to the  $\text{Fe}^{3+}$  charge transfer band.

Indeed, neutron activation analysis indicated that there was about 250 ppm of Fe present.

Defects resulting from TCR of MgO at high temperatures are primarily anion vacancies. Anion vacancies occur in two charge states,  $F^+$  and  $F$  centers, corresponding to vacancies with one and two electrons, respectively. Both of these defects absorb at about 4.9 eV.<sup>10</sup> The concentration of anion vacancies can be estimated using the formula<sup>11</sup>

$$n(F) = 5 \times 10^{15} \alpha(F),$$

where  $n(F)$  denotes the concentration of anion vacancies and  $\alpha(F)$  is the absorption coefficient of the 4.9-eV band. The estimated concentration was  $2.7 \times 10^{17} \text{ cm}^{-3}$  (Table II).

In addition, a broad band centered at about 3.1 eV ap-

TABLE I. Chemical analyses of Norton, Muscle-Shoals, Tateho, Spicer, and Oak Ridge (MgO) crystals.

Element	Norton ( $\mu\text{g/g}$ )	Muscle-Shoals ( $\mu\text{g/g}$ )	Tateho ( $\mu\text{g/g}$ )	Spicer ( $\mu\text{g/g}$ )	OR ( $\mu\text{g/g}$ )
Ag					<1
Al	21	27	33	41	6
As				<0.4	
B					<2
Ba				<0.6	<3
Be					<1
Bi					<3
Ca				61	14
Cl		18	8		
Co					<10
Cr	11	21	16	<5	1
Cu					<1
Fe	245	112	140	3	2
Ge					<5
Hf	4				
In		0.2			
K		43			<5
Li					<1
Mn	31	7	4	0.3	~0.06
Mo					<1
N				9	7
Na 80		74	77	0.3	0.7
Ni		96	77	<5	
P				2	5
Pb				0.5	<5
Rb					<5
S				<2	<5
Sb					<5
Si				19	14
Sn					<3
Sr					<5
Ti					2
V	1	3	11		<3
Yb			0.3		
Zr	114			<6	<4

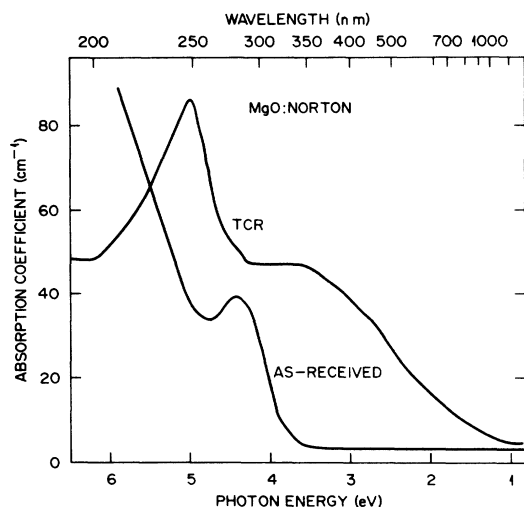


FIG. 1. Optical-absorption spectra of MgO (N) crystals before and after thermochemical reduction.

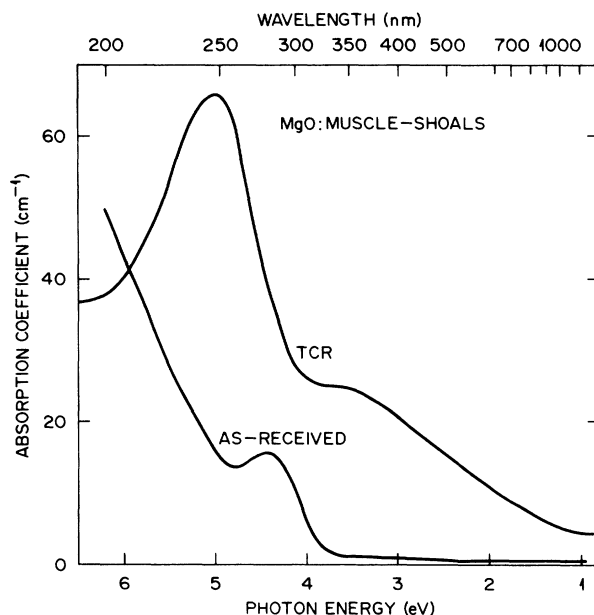


FIG. 2. Optical-absorption spectra of MgO (MS) crystals before and after thermochemical reduction.

peared. This broadband appeared to be more pronounced when the crystal was impure. The MgO (MS) and MgO (T) crystals also have large absorption bands at 290 nm (Figs. 2 and 3). After TCR, bands at 4.9 and 3.1 eV appeared. The corresponding anion vacancy concentrations are given in Table II.

The  $\text{Fe}^{3+}$  concentration in MgO (S) and MgO (OR) was lower than in the other three crystals (Table II). The intensities of the corresponding precipitate band at 3.1 eV were much lower, as is shown in Figs. 4 and 5.

### 2. Luminescence spectra

All the MgO crystals contained chromium to a greater or lesser extent (Table I). The absorption band due to  $\text{Cr}^{3+}$  peaks at about 440 nm (2.8 eV).<sup>12</sup> In our samples, the  $\text{Cr}^{3+}$  concentration was too low to be monitored by the absorption at 440 nm. However, luminescence is much more sensitive than absorption. Figure 6 shows the luminescence spectra of the three samples with higher  $\text{Cr}^{3+}$  concentration. The thickness of the samples was 0.4 mm. The luminescence intensity reflects the  $\text{Cr}^{3+}$  content in the samples (Table I). The luminescence intensities from MgO (S) and MgO (OR) were much lower than those of the other three and were not plotted.

## C. Electron microscopy observations

### 1. Precipitates

As-grown crystals of nominally pure MgO contained no precipitates down to the visibility limit of about 1 nm for diffraction contrast imaging. As mentioned before, after the high-temperature reducing treatment, the specimens darkened. The reduction was found to start from the surface of the specimens,<sup>4</sup> so the reduction time of three hours was long enough to achieve a uniform distribution of precipitates throughout the entire sample. Nevertheless, the concentration of precipitates appeared to be higher in the surface region.

(a) *MgO (N) crystals.* Figure 7 shows a typical electron micrograph from reduced MgO (N) specimens. The black spots represent precipitates, the average size and concentration of which were determined to be 45 nm and  $1.2 \times 10^{13} \text{ cm}^{-3}$ , respectively. The structure of the precipitates was investigated by the microdiffraction technique. Microdiffraction with a finite incident beam divergence produces diffraction patterns that consist of disks.

TABLE II. Crystal designation, optical characterization, and TEM results on the five TCR crystals.

Sample source	MgO (N) Norton	MgO (MS) Muscle-Shoals	MgO (T) Tateho	MgO (S) Spicer	MgO (OR) Oak Ridge
$\alpha(4.3 \text{ eV})$	25.1	9.0	3.0	2.6	0.6
$n(\text{Fe}^{3+})$ (ppm)	70	27	9	8	1.5
$\alpha(4.9 \text{ eV})$	53	42	49	28	28
$n(F)$ ( $\text{cm}^{-3}$ )	$2.7 \times 10^{17}$	$2.1 \times 10^{17}$	$2.4 \times 10^{17}$	$1.4 \times 10^{17}$	$1.4 \times 10^{17}$
$\alpha(3.1 \text{ eV})$	21	10	5	<2	<1
Precipitate size (nm)	45	35	45	<10	<10

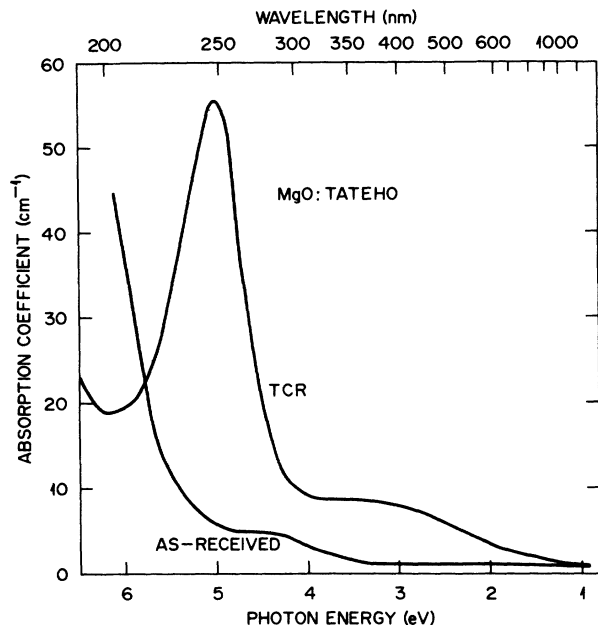


FIG. 3. Optical-absorption spectra of MgO (T) crystals before and after thermochemical reduction.

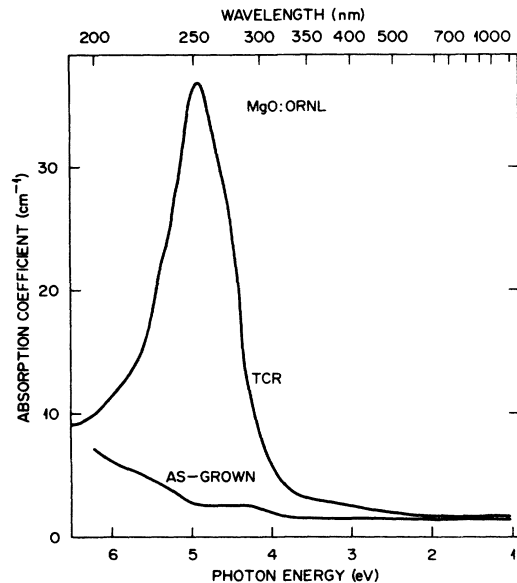


FIG. 5. Optical-absorption spectra of MgO (OR) crystals before and after thermochemical reduction.

A pattern of this type is shown in Fig. 8, which was obtained from a precipitate embedded in the matrix. It therefore contained matrix as well as precipitate reflections, and from a number of such patterns the crystallographic relationship between the matrix and the precipitate was determined. Using the MgO matrix spots as an internal calibration, the precipitate reflections were found to correspond to a fcc crystal structure with a lattice constant of  $a_0 = 3.61 \pm 0.02 \text{ \AA}$ , essentially the same as that of bulk fcc iron in the  $\gamma$  phase. The following crystallographic relationship between the matrix and the fcc precipitates was found:

$$\langle 001 \rangle_p \parallel \langle 001 \rangle_m ,$$

$$\langle 010 \rangle_p \parallel \langle 010 \rangle_m .$$

A few precipitates exhibited moiré fringes (such as the precipitate next to the arrow in Fig. 7). The moiré fringe spacing of  $63 \text{ \AA}$  was not consistent with a fcc precipitate structure, but was consistent with a bcc precipitate having an orientation relationship with the matrix of

$$\langle 011 \rangle_p \parallel \langle 001 \rangle_m .$$

X-ray microanalysis was also performed on precipi-

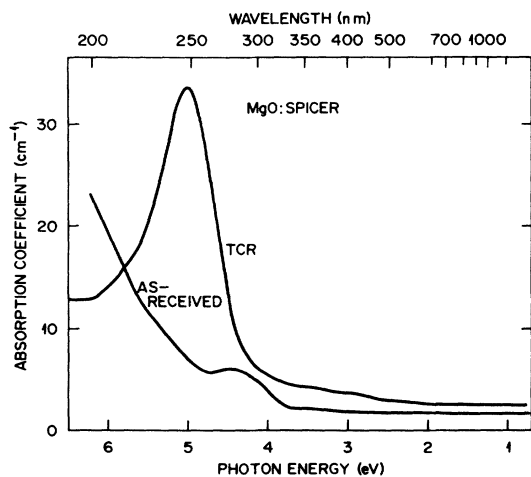


FIG. 4. Optical-absorption spectra of MgO (S) crystals before and after thermochemical reduction.

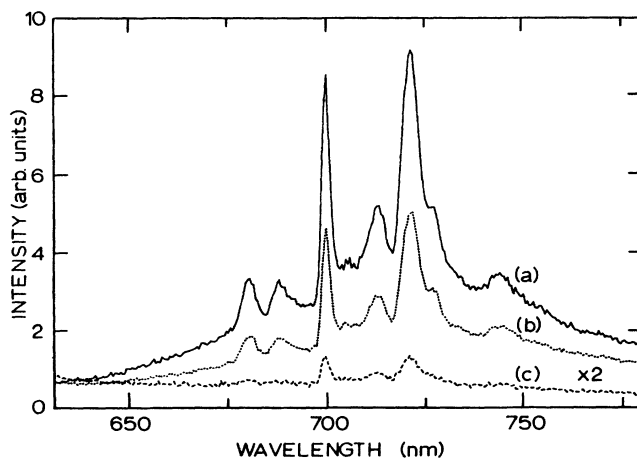


FIG. 6. Chromium luminescence spectra in (a) MgO (MS), (b) MgO (T), and (c) MgO (N) samples.

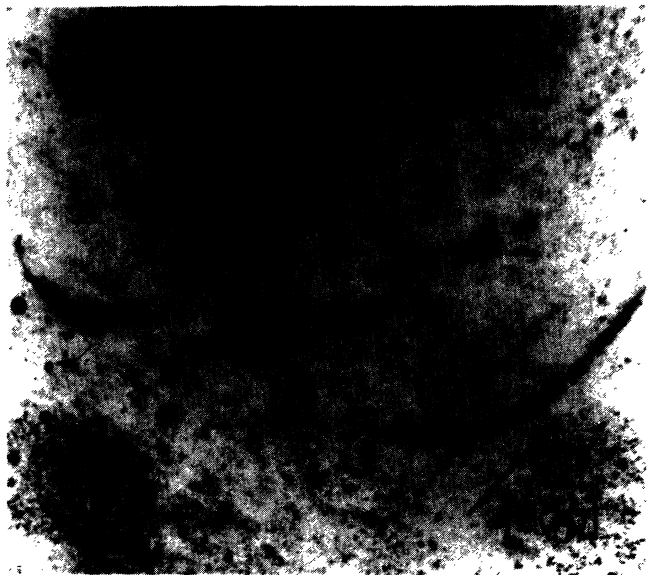


FIG. 7. Electron micrograph showing the iron precipitates in a MgO (N) specimen.

tates embedded in the matrix using the small convergent probe. Figure 9 shows a typical x-ray fluorescence spectrum from the precipitate with Fe  $K\alpha$  and Fe  $K\beta$  lines. The very intense line on the low-energy side corresponds to  $K$  lines of the Mg in the matrix. In some of the precipitates a Cr concentration of  $\sim 1\%$  was also determined.

(b) *MgO (MS) crystals.* Electron microscopy observations in MgO (MS) crystals after TCR indicated that the distribution of precipitates was very inhomogeneous, and areas with a concentration of about  $10^{13}$  precipitates/cm<sup>3</sup>

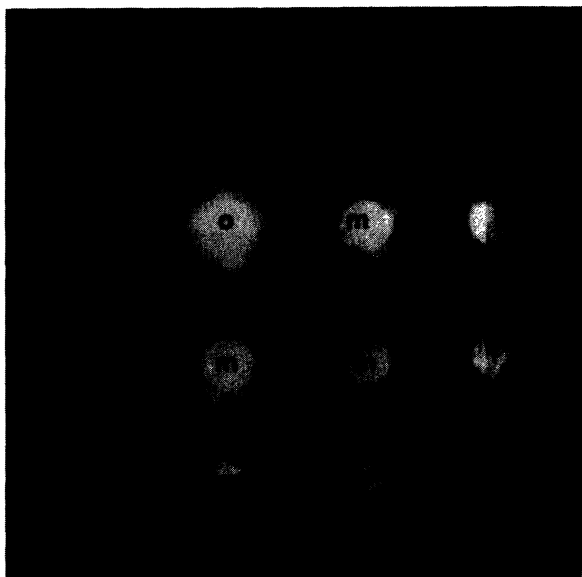


FIG. 8. Microdiffraction pattern from a fcc precipitate in a MgO (N) specimen, showing the unscattered beam (*o*), the matrix spots (*m*), and the precipitate spots (*p*).

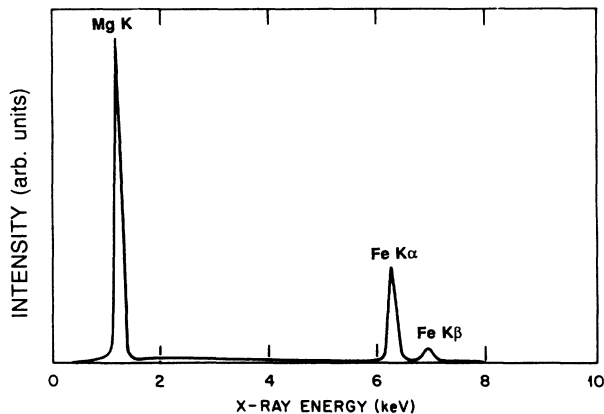


FIG. 9. Energy-dispersive x-ray fluorescence spectrum from an Fe precipitate in MgO (N) showing the Fe  $K\alpha$  and Fe  $K\beta$  peaks and a very intense peak of Mg from the matrix.

were separated from regions which were almost free from precipitates [Fig. 10(a)]. For this reason, the total precipitate concentration was not measured. The average size was determined to be 35 nm. Occasionally, larger precipitates with a size of about 70 nm were also imaged [Fig. 10(b)]. Thickness fringes were observed in these large precipitates.

Microdiffraction patterns (Fig. 11) indicate that the reflections associated with the precipitates in general

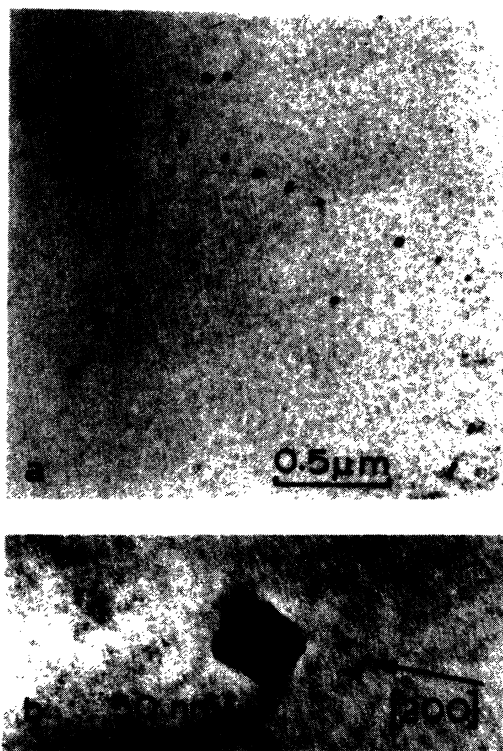


FIG. 10. Electron micrograph showing the iron precipitates in (a) a MgO (MS) specimen, and (b) large precipitate showing thickness fringes.



FIG. 11. Microdiffraction pattern from a bcc precipitate in a MgO (MS) specimen, showing the unscattered beam (*o*), the matrix spots (*m*), and the precipitate spots (*p*).

correspond to a bcc crystal structure with a lattice constant of  $a_0 = 2.89 \pm 0.06 \text{ \AA}$ , essentially the same as that of bulk bcc iron (the  $\alpha$  phase). Precipitates with a fcc structure and a lattice constant of  $a_0 = 3.61 \text{ \AA}$  were occasionally found. This latter value is close to that of the fcc iron ( $\gamma$  phase). The following crystallographic relationship between matrix and precipitates was found:

$$\begin{aligned} \langle 001 \rangle_p \parallel \langle 001 \rangle_m, \quad \langle 110 \rangle_p \parallel \langle 010 \rangle_m \quad \text{for bcc,} \\ \langle 001 \rangle_p \parallel \langle 001 \rangle_m, \quad \langle 010 \rangle_p \parallel \langle 010 \rangle_m \quad \text{for fcc.} \end{aligned}$$

X-ray microanalysis of the precipitates indicated the presence of Fe as well as Cr. Figure 12 shows a typical x-ray fluorescence spectrum from the precipitates. It ex-

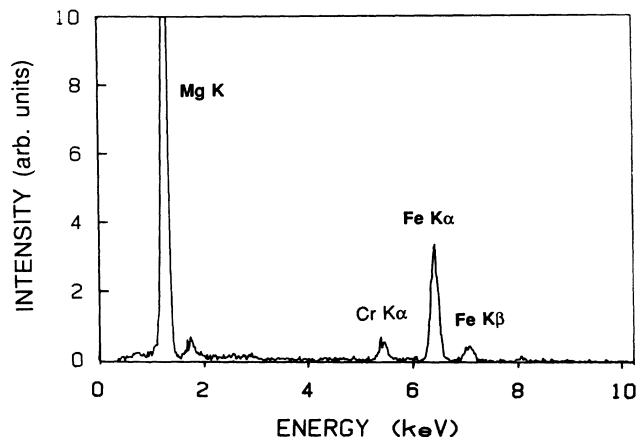


FIG. 12. Energy-dispersive x-ray fluorescence spectrum from an Fe-Cr precipitate in MgO (MS) showing the Fe  $K\alpha$  and Fe  $K\beta$  lines together with the Cr  $K\alpha$  line.

hibited the Fe  $K\alpha$  and Fe  $K\beta$  lines together with the Cr  $K\alpha$  and the Cr  $K\beta$  lines. The small peak on the right of the Mg  $K$  matrix line is a Ta  $M$  line due to the specimen support ring. The relative Fe and Cr concentrations were analyzed using x-ray generation constants computed by a standardless method.<sup>13</sup> The concentration of iron in the precipitates ranged from 90% to 75% and that of chromium from 10% to 25%. All the precipitates with a fcc structure had a Cr content smaller than 18%.

The Fe-Cr precipitates with bcc structure can correspond to the  $\alpha$  phase of the Fe-Cr alloy. This phase appears on cooling down the alloy from the melt.<sup>14,15</sup> Its lattice constant has a value of  $a_0 = 2.86 \text{ \AA}$ , close to our value of  $a_0 = 2.89 \pm 0.06 \text{ \AA}$ . The closed fcc loop of the Fe-Cr solid solution is thought to extend to about 12 at. % Cr.<sup>14</sup>

(c) *MgO (T) crystals.* In thermochemically reduced Tateho crystals, precipitates appeared concentrated at the subgrain boundaries (Fig. 13). The formation of precipitates at the sub-boundary dislocations is a normal occurrence in ionic crystals because of the elastic and electronic potentials associated with the dislocations. The average size of the precipitates was determined to be  $\sim 45 \text{ nm}$ .

Microdiffraction patterns indicated that the precipitates possessed a bcc crystal structure with a lattice constant of  $a_0 = 2.89 \pm 0.06 \text{ \AA}$ . The crystallographic relationships between matrix and precipitates were the same as those found for bcc precipitates in MgO (MS) crystals. From a Moiré fringe spacing of  $53 \text{ \AA}$  [Fig. 13(a)], using a

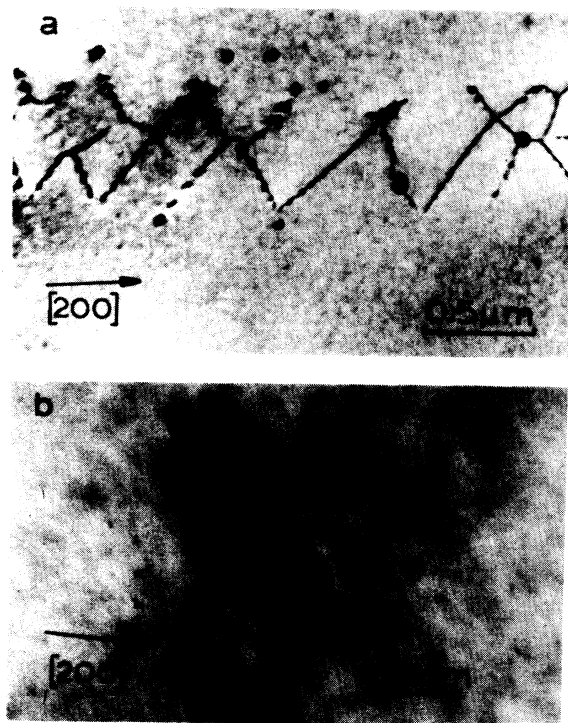


FIG. 13. Electron micrographs showing (a) the precipitates at a subgrain boundary in a MgO (T) crystal, (b) moiré pattern from precipitate and matrix planes.

matrix  $\{200\}$  spacing of 2.107 Å, the  $\{110\}$  spacing of the precipitate was calculated to be 2.026 Å. This corresponds to  $a_0 = 2.865$  Å, in good agreement with the value obtained from the diffraction patterns. These values also agree with those of the bcc precipitates in MgO (MS) crystals.

X-ray microanalysis of the precipitates again indicated the presence of Fe and Cr. Quantitative microanalysis gave a Cr concentration smaller than 6%.

(d) *MgO (S) and MgO (OR) crystals.* In TCR crystals from Spicer or Oak Ridge, the precipitate concentration was very small,  $\leq 10^{12}$  precipitates/cm<sup>3</sup>. The average size of the precipitates was also small, about 10 nm. The microdiffraction patterns could not be obtained. X-ray microanalysis indicated that the precipitates were Fe precipitates with a Cr concentration of less than 0.1%.

## 2. Dislocation loops

Dislocation loops were found in all TCR crystals. In this section, we report our TEM studies on dislocation loops in a sample thermochemically reduced for one hour at  $\sim 1900$  K and fast cooled.

Figure 14 shows a typical electron micrograph taken under bright field kinematical conditions using the diffraction vector  $g = \langle 200 \rangle$ . Dislocation loops were observed lying in  $\{100\}$  planes and having  $a\langle 100 \rangle$  Burgers vectors. Considering all types of loops, the average size and the density of loops is 150 nm and  $2 \times 10^{12}$  cm<sup>-3</sup>, respectively. The nature (vacancy or interstitial) of the dislocation loops was determined by the inside-outside contrast method.<sup>16-18</sup> Since the lattice rotations introduced by vacancy and interstitial loops are of opposite nature the inside-outside contrast under the same geometric circumstances will also be of opposite nature. All of the analyzed loops were found to be vacancy type.

Vacancy dislocation loops in plastically deformed MgO have  $a/2\langle 110 \rangle$  Burgers vectors and lie in  $\{100\}$  planes;<sup>19-21</sup> their average size is 150 nm. During defor-

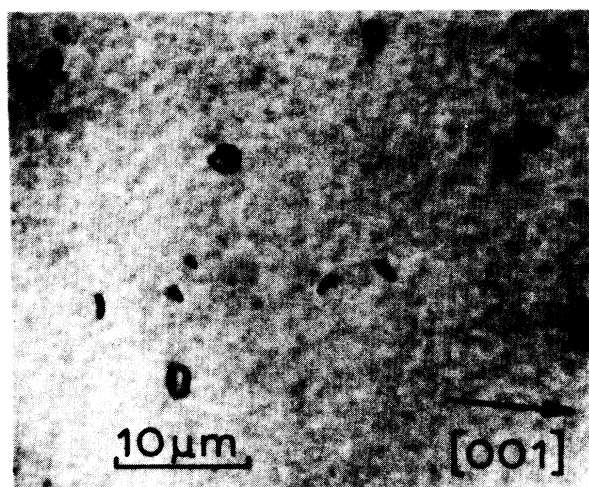


FIG. 14. Bright field electron micrograph under kinematical diffraction conditions dislocation loops in a MgO (OR) specimen.

mation, the loops are formed primarily from dislocation dipoles which are created by joggling of slip dislocations. Since at low temperatures only the  $\langle 110 \rangle \{110\}$  slip system is active, the loops are restricted to have  $(a/2)\langle 110 \rangle$  type Burgers vectors. Vacancy dislocation loops of a  $\langle 100 \rangle$  Burgers vectors lying  $\{100\}$  planes have been observed in electric-field treated specimens<sup>22,23</sup> at temperatures greater than or equal to 1273 K. The average size of the loops was 35 nm. It has been proposed that these loops can presumably be formed as a result of condensation of vacancies that are created during electric-field treatment.<sup>23</sup> Also, precipitates have been observed after electric-field treatments.<sup>24</sup> In TCR crystals there exists a high concentration of anion vacancies. It is possible that condensation of these vacancies caused the formation of the large loops observed in TCR samples.

## IV. SUMMARY AND CONCLUSIONS

MgO crystals from five sources, with varying impurity contents, were thermochemically reduced at high temperatures. Anion vacancies were formed, as evidenced by the presence of an absorption band at 4.9 eV. A broad extinction in the visible region was also observed. It was responsible for the dark appearance of the crystals. This coloration is obviously impurity dependent since impure crystals were darker in color. A combined optical and analytical transmission-electron-microscopy study indicated that the dark coloration was due to Mie scattering from metallic precipitates in the crystals. The precipitates were characterized by using analytical transmission electron microscopy. These results established that the precipitates were primarily Fe in content, although Fe precipitates with a Cr concentration up to about 25% were also observed. Microdiffraction patterns show that the precipitates possess the fcc or bcc structure with lattice constants of  $a_0 = 3.71 \pm 0.02$  Å and  $a_0 = 2.89 \pm 0.06$  Å, respectively. The fcc precipitates exhibit a  $\langle 001 \rangle_p \parallel \langle 001 \rangle_m$ ,  $\langle 010 \rangle_p \parallel \langle 010 \rangle_m$  precipitate-matrix orientation relationship. The bcc precipitates have a  $\langle 001 \rangle_p \parallel \langle 001 \rangle_m$ ,  $\langle 110 \rangle_p \parallel \langle 010 \rangle_m$  relationship. We have further established from chemical analyses, optical measurements, and transmission electron microscopy that the greater the transition-metal impurity content the larger are the dimensions and number density of the precipitates.

## ACKNOWLEDGMENTS

The authors are indebted to M. M. Abraham for his assistance in the growth of the high-purity crystals and helpful discussions. This research was sponsored by the Defense Advanced Research Projects Agency under Interagency Agreement 40-1611-85 with Martin Marietta Energy Systems, Inc., Contract No. DE-AC05-84OR21400 with the U.S. Department of Energy. Two of us (C.B. and R.G.) wish to acknowledge the support of the Comisión Asesora de Investigación Científica y Técnica of Spain.

- <sup>1</sup>Y. Chen and R. González, *Opt. Lett.* **10**, 276 (1985), and references therein.
- <sup>2</sup>B. Henderson and R. D. King, *Philos. Mag.* **13**, 1149 (1966).
- <sup>3</sup>Y. Chen, R. T. Williams, and W. A. Sibley, *Phys. Rev.* **182**, 960 (1969).
- <sup>4</sup>J. Narayan, Y. Chen, R. M. Moon, and R. N. Carpenter, *Philos. Mag. A* **49**, 287 (1984).
- <sup>5</sup>R. M. Bunch, W. P. Unruh, and M. V. Iverson, *J. Appl. Phys.* **58**, 1474 (1985).
- <sup>6</sup>M. S. Corisco, R. Gonzalez, and C. Ballesteros, *Philos. Mag. A* **52**, 669 (1985).
- <sup>7</sup>M. M. Abraham, C. T. Butler, and Y. Chen, *J. Chem. Phys.* **55**, 3752 (1971).
- <sup>8</sup>Y. Chen, D. L. Trueblood, O. E. Schow, and H. T. Tohver, *J. Phys. C* **3**, 2501 (1970).
- <sup>9</sup>R. W. Carpenter, J. Bentley, and E. A. Kenik, *Scanning Electron Microscopy* (IIT Research Institute, Chicago, 1977). Vol. 1, p. 411.
- <sup>10</sup>Y. Chen, J. L. Kolopus, and W. A. Sibley, *Phys. Rev.* **182**, 960 (1969).
- <sup>11</sup>W. A. Sibley and Y. Chen, *Phys. Rev.* **160**, 712 (1967).
- <sup>12</sup>D. S. McClure, *J. Chem. Phys.* **36**, 2757 (1962).
- <sup>13</sup>N. J. Zaluzec, *Introduction to Analytical Electron Microscopy*, edited by J. Hren, J. Goldstein, and D. Joy (New York, Plenum, 1979), p. 121.
- <sup>14</sup>W. B. Pearson, *Handbook of Lattice Spacings and Structures of Metals and Alloys* (Pergamon, New York, 1958), p. 532.
- <sup>15</sup>M. Hansan, *Constitution of Binary Alloys* (McGraw-Hill, New York, 1958), p. 525.
- <sup>16</sup>D. N. Maher and B. L. Eyre, *Philos. Mag.* **23**, 409 (1971).
- <sup>17</sup>P. B. Hirsch, A. Howie, R. B. Nicholson, B. W. Pashley, and M. J. Whelan, in *Electron Microscopy of Thin Crystals* (Butterworths, London, 1965), p. 254.
- <sup>18</sup>H. Föll and M. Wilkens, *Phys. Status Solidi A* **31**, 519 (1975).
- <sup>19</sup>G. W. Groves and A. Kelly, *Philos. Mag.* **6**, 1527 (1961); **7**, 892 (1962).
- <sup>20</sup>J. Washburn, in *Electron Microscopy and Strength of Crystals*, edited by G. Thomas and J. Washburn (Interscience, New York, 1963), p. 301.
- <sup>21</sup>J. Narayan and J. Washburn, *Philos. Mag.* **26**, 1179 (1972).
- <sup>22</sup>J. Narayan, R. A. Weeks, and E. Sonder, *J. Appl. Phys.* **49**, 5977 (1978).
- <sup>23</sup>J. Narayan, *J. Appl. Phys.* **57**, 2703 (1985).
- <sup>24</sup>M. M. Abraham, L. A. Boatner, W. H. Christie, F. A. Modine, T. Negas, R. M. Bunch, and W. P. Unruh, *J. Solid State Chem.* **51**, 1 (1984).

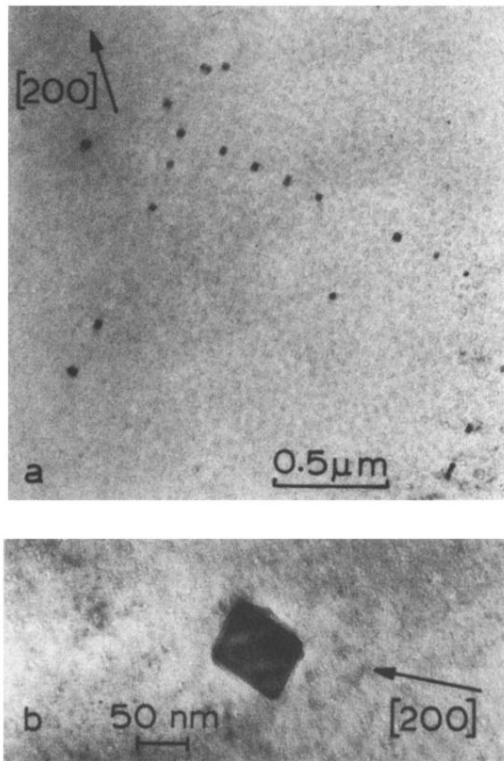


FIG. 10. Electron micrograph showing the iron precipitates in (a) a MgO (MS) specimen, and (b) large precipitate showing thickness fringes.

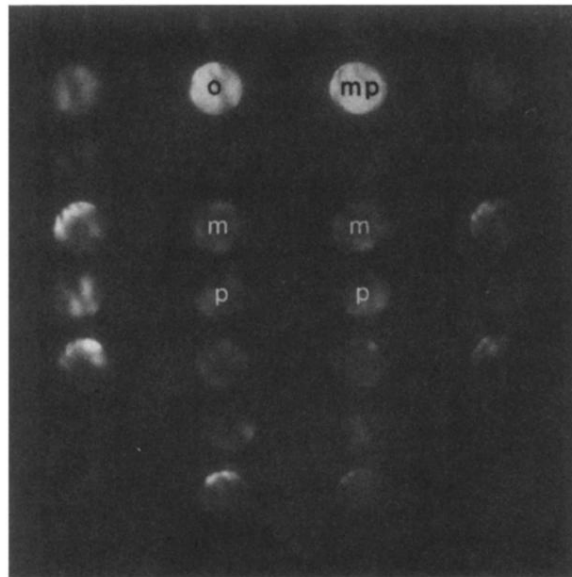


FIG. 11. Microdiffraction pattern from a bcc precipitate in a MgO (MS) specimen, showing the unscattered beam (*o*), the matrix spots (*m*), and the precipitate spots (*p*).

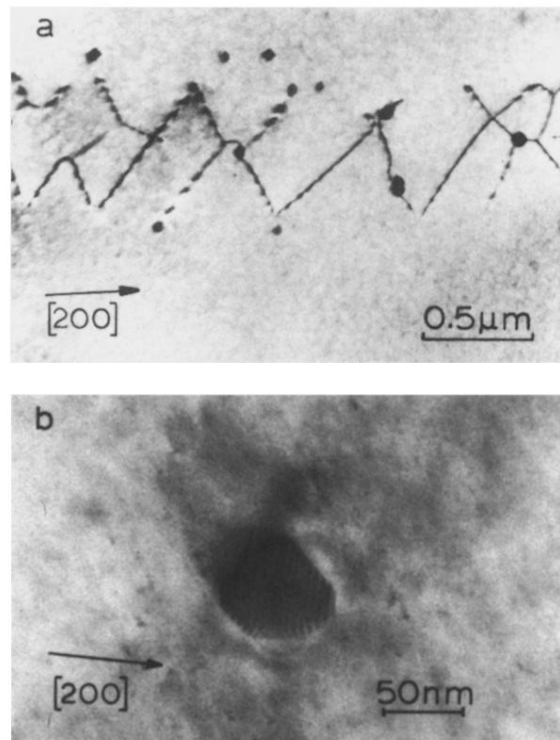


FIG. 13. Electron micrographs showing (a) the precipitates at a subgrain boundary in a MgO (T) crystal, (b) moiré pattern from precipitate and matrix planes.

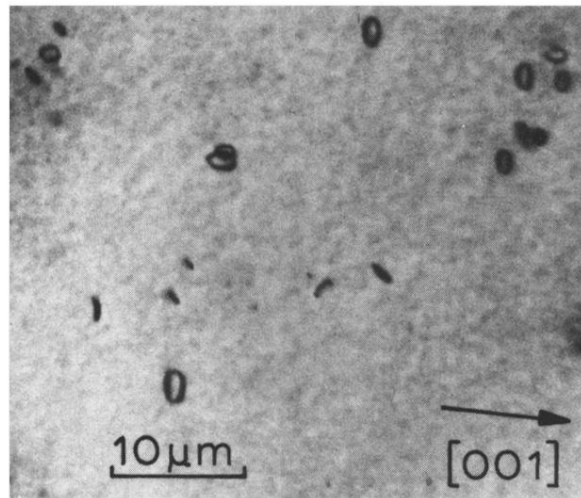


FIG. 14. Bright field electron micrograph under kinematical diffraction conditions dislocation loops in a MgO (OR) specimen.

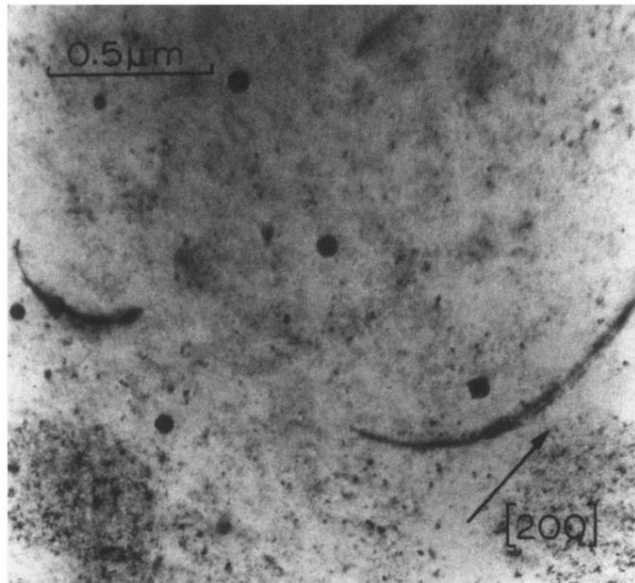


FIG. 7. Electron micrograph showing the iron precipitates in a MgO (N) specimen.

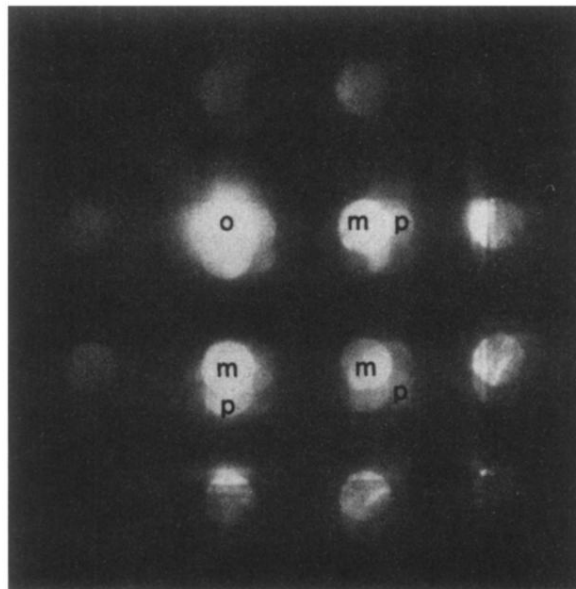


FIG. 8. Microdiffraction pattern from a fcc precipitate in a MgO (N) specimen, showing the unscattered beam (*o*), the matrix spots (*m*), and the precipitate spots (*p*).